

Shock and Discontinuity Formation in the Front of an Expanding Coronal Magnetic Arcade in Two-Fluid Simulations

T.E. BAGWELL¹ AND Z.W. MA¹

¹*Institute for Fusion Theory and Simulation, Department of Physics, Zhejiang University, Hangzhou 310027, P.R.China*

ABSTRACT

The dynamic evolution of a magnetic arcade associated with photospheric shearing motions is investigated by an ideal two-fluid (electron-ion) code. The two-fluid numerical simulations produce conspicuous differences compared to earlier MHD simulations beyond the inner arcade region. The decoupling motion between electrons and heavier ions during the arcade expansion induces a growing charge separation and strong electric field in the front of the expanding arcade. The presence of this electric field provides an additional force, along with the magnetic and thermal pressures, that drive the growth of an outwardly expanding wave that steepens into a propagating discontinuity in the plasma and magnetic field. The propagation speed of the discontinuity eventually exceeds the local phase velocity of the MHD fast mode and becomes a perpendicular fast-like shock. Preferential heating of the ions is also observed. In addition, parameter tests indicate that (1) the propagation speed of the shock is independent of the maximum shear speed; (2) slower shearing speeds produce weaker shocks with weaker adiabatic heating; (3) the ion to electron mass ratio, m_i/m_e , impacts the strength of the charge separation linearly, but has a moderate effect on the propagation speed; and (4) the normalized value of the ion inertial length does not affect the formation and the speed of the shock as a whole.

Keywords: shock – discontinuity – solar corona – magnetic arcades – multi-fluid

1. INTRODUCTION

Sheared magnetic arcades forming highly non-potential magnetic fields are regarded as candidates for the origins of solar eruptive events (other candidates include non-zero magnetic helicity flux ropes and flux emergence regions) and are considered a quintessential type of storage models for coronal mass ejections (CMEs) and flares (Forbes 2000; Klimchuk 2001). The arcades accumulate magnetic free energy as their footpoints at the photosphere undergo slow shearing motions. It is typically assumed that the coronal arcades react passively to this photospheric motion and their evolution is considered quasi-static because of the relatively rapid speed of information transfer along the field lines ($\sim 1000 \text{ km s}^{-1}$) compared to the much slower photospheric perturbations ($\sim 1 \text{ km s}^{-1}$) coupled with the small value of the plasma β in the corona. In original shearing arcade models, magnetic free energy was thought to be stored purely in force-free, or

field-aligned, currents within simply-connected force-free magnetic field structures. However, papers by Aly (1984) and Sturrock (1991) had demonstrated that for simply-connected force-free fields, the magnetic energy is always greater after the field has fully-opened, matching the fields observed directly after the eruption of CMEs, compared to the initial, closed-lined field having the same boundary flux distribution at the photosphere, thus giving rise to an apparent energy paradox. Then Mikić, Barnes, & Schnack (1988) were the first to demonstrate through resistive magnetohydrodynamic (MHD) numerical simulations that shearing arcades also stored energy in the form of thinning current sheets that led to magnetic reconnection and the rapid change in magnetic topology with the release of magnetic energy and the ejection of a plasmoid; therefore avoiding the Aly-Sturrock condition for simply-connected fields. Later, Mikić & Linker (1994) showed in simulations that a single magnetic arcade undergoing purely shearing motions in a spherical geometry could also give rise to a strong current layer that becomes the site of magnetic reconnection producing events that are morphologically similar to those observed in CMEs and flares. Other two-dimensional MHD numerical studies have since con-

firmed this behavior of a single arcade (Amari et al. 1996; Choe & Lee 1996b). The simulations show that as the distance between conjugate footpoints increases due to antiparallel shearing motions at the photosphere, the arcade expands outwards and the central field lines of the arcade begin to stretch vertically. Opposite polarity field lines are pinched closer together laterally eventually forming a strong current sheet in the central arcade. After reaching a critical amount of shear, spontaneous magnetic reconnection is triggered due to the locally enhanced dissipation and the magnetic tension associated with reconnected magnetic field propels the ejection of a plasmoid. This topological change seen in simulations is similar to observations of some solar flare events where X-shaped structures are seen at the tops of flare loops (Masuda et al. 1994).

Developments in the two-fluid theory of magnetic reconnection give a more accurate picture of magnetic reconnection compared to MHD theory. The MHD theory of magnetic reconnection should not be applied to regions with a thin current layer where the ions, due to their large cyclotron orbits, become demagnetized while the electrons remain strongly magnetized producing distinct two-fluid motions (Yamada et al. 2010). Therefore the flux annihilation seen in thin current layers occurs on a length scale intermediate between the ion inertial length d_i and electron skin depth d_e , so there is no guarantee that the velocities of the ions and electrons are nearly the same as assumed by MHD, therefore two-fluid dynamics become important. The increased thinning of a current sheet seen in two-fluid models of magnetic reconnection and the distinct differential motions of the ions and electrons can produce strong reconnection electric fields that increase the reconnection rate beyond that predicted by Sweet-Parker theory which is important in collisionless plasmas, like those in solar coronae and planetary magnetospheres (Ma & Bhattacharjee 1996; Biskamp, Schwarz, Drake 1995). Two-fluid effects in the reconnection layer of arcades in solar coronae could account for certain observational features of solar eruptive events. For instance, two-fluid reconnection can produce stronger current sheet thinning thereby enhancing the typical tearing-mode that could cause the creation of multiple plasma blobs in the thin current sheet and reconnection regions and the expulsion of plasma ejecta in the outflow regions, which have been observed in recent observations (Takasao et al. 2012; Zhang & Li 2019).

Shock waves in collisionless coronal plasmas are also manifested by two-fluid and kinetic effects since in collisionless plasmas the spatial characteristics of the shocks in collisionless plasmas are not determined by the mean-

free path, such as in typical hydrodynamic shocks, but by other length scales like the ion and electron cyclotron radii. These effects have occupied research on coronal heating and the characteristics of the solar wind for decades and the two phenomena may be intricately related (Kuperus et al. 1981). The origin of these shocks observed in the corona are thought to be produced in two main ways: (1) by impulsive solar events generated by magnetic reconnection and microflares (Hsieh et al. 2009) and (2) by the propagation of Alfvén waves due to perturbations originating from the lower solar atmosphere that steepen into shocks as they propagate into the higher, more tenuous corona (Osterbrock 1961; Orta et al. 2003). Two-fluid and kinetic effects are also important for explaining the preferential heating of ions in collisionless shocks (Zimbaro 2011; Lee & Wu 2000).

At present it is impossible practically in a two-fluid code to produce a computational gridding that is able to resolve the real ion inertial length d_i , the length scale where ion and electron motions decouple, of the solar corona while also simulating the real global length scale of solar magnetic arcades as they differ by many orders of magnitude. Therefore, a two-fluid simulation whose length scale is normalized to d_i could at best produce qualitative results in a practical amount of time by artificially increasing d_i and ensuring that the adopted ion inertial length, d_i , remains much smaller than the global length scale of the magnetic arcade and coronal structure l_0 , simulated, i.e., $l_0 \gg d_i$. This manipulation of the ion inertial length is performed for the simulations in this paper. We performed several simulations for the purpose of convergent analysis with varying adopted values of the artificially increased d_i and observed nearly identical behavior across the simulations. Therefore, we feel confident that as long as d_i remains much smaller than the global scale l_0 , the simulations performed in the present study still retain physical authenticity with the evolution of a full-size, completely resolved magnetic arcade system. In our two-fluid simulations, it is found that before the current sheet and impulsive magnetic reconnection could occur, as observed in the simulations by (Choe & Lee 1996a,b), propagating discontinuities and shocks have formed at the periphery of the expanding arcade and unperturbed plasma that occurs with a strong breakdown of local charge neutrality and are driven by the mild photospheric shearing motions at the base.

The outline of the present paper is as follows. In §2, the two-fluid model and governing equations are introduced along with the initial and boundary conditions adopted for simulating the evolution of a y -invariant magnetic arcade being sheared by photospheric flow.

The numerical results are presented in §3 with two subsections, the first subsection describes the results of a representative case that are qualitatively general across all of the simulations undertaken, while in the second subsection the results of a set of parameter tests are reported and discussed. Lastly in §4, we conclude and summarize the results of the present study.

2. NUMERICAL TWO-FLUID MODEL

2.1. Governing Equations

A ideal two-fluid code is developed to study the dynamic evolution of the solar corona while the footpoints of a magnetic arcade undergo slow shearing motions. We reframe the MHD system used by [Choe & Lee \(1996a\)](#) directly into a two-fluid model framework, this facilitates direct comparisons of the numerical results between the MHD model of [Choe & Lee \(1996a\)](#) and the two-fluid model used in this study. In our model, all physical variables depend only on the horizontal coordinate x and the vertical coordinate z and are assumed to be invariant in the y -direction ($\partial/\partial y = 0$) in the Cartesian coordinate system. The corona itself occupies the half-space $z > 0$. The governing equations are a set of ideal two-fluid equations including gravity that consists purely of ions and electrons, while no neutral particles are assumed. In order to simulate the ideal evolution, no resistive terms are included, therefore interactions between the ion and electron fluids are mediated purely through the electromagnetic fields. In addition, the thermodynamics of the ion and electron fluids are assumed to be purely adiabatic, no auxiliary conduction, heating, nor cooling terms are included. The governing equations, after normalization, are as follows (ion and electron quantities are denoted by the subscripts i and e , respectively):

$$\frac{\partial n_i}{\partial t} = -\nabla \cdot (n_i \mathbf{v}_i), \quad (1)$$

$$\frac{\partial n_i \mathbf{v}_i}{\partial t} = -\nabla \cdot (n_i \mathbf{v}_i \mathbf{v}_i + p_i \bar{\mathbf{I}}) + n_i (\mathbf{E} + \mathbf{v}_i \times \mathbf{B}) + n_i \mathbf{g}, \quad (2)$$

$$\frac{\partial \epsilon_i}{\partial t} = -\nabla \cdot [(\epsilon_i + p_i) \mathbf{v}_i] + n_i \mathbf{v}_i \cdot \mathbf{E} + n_i \mathbf{v}_i \cdot \mathbf{g}, \quad (3)$$

$$\frac{\partial n_e}{\partial t} = -\nabla \cdot (n_e \mathbf{v}_e), \quad (4)$$

$$\frac{\partial n_e \mathbf{v}_e}{\partial t} = -\nabla \cdot \left(n_e \mathbf{v}_e \mathbf{v}_e + \frac{m_i}{m_e} \tilde{p}_e \bar{\mathbf{I}} \right) - \frac{m_i}{m_e} n_e (\mathbf{E} + \mathbf{v}_e \times \mathbf{B}) + \tilde{n}_e \mathbf{g}, \quad (5)$$

$$\frac{\partial \epsilon_e}{\partial t} = -\nabla \cdot [(\epsilon_e + p_e) \mathbf{v}_e] - n_e \mathbf{v}_e \cdot \mathbf{E} + \frac{m_e}{m_i} n_e \mathbf{v}_e \cdot \mathbf{g}, \quad (6)$$

$$\frac{\partial \psi}{\partial t} = E_y, \quad (7)$$

$$\frac{\partial B_y}{\partial t} = \frac{\partial E_z}{\partial x} - \frac{\partial E_x}{\partial z}, \quad (8)$$

$$\frac{\partial \mathbf{E}}{\partial t} = \left(\frac{c}{v_0} \right)^2 [\nabla \times \mathbf{B} - (n_i \mathbf{v}_i - n_e \mathbf{v}_e)], \quad (9)$$

$$B_x = \frac{\partial \psi}{\partial z}, \quad B_z = -\frac{\partial \psi}{\partial x}, \quad (10)$$

$$p_i = n_i k_B T_i, \quad p_e = n_e k_B T_e \quad (11)$$

where the ion and electron energies are defined as $\epsilon_i = \frac{1}{2} n_i v_i^2 + \frac{p_i}{\gamma-1}$ and $\epsilon_e = \frac{1}{2} \frac{m_e}{m_i} n_e v_e^2 + \frac{p_e}{\gamma-1}$, respectively, with $\gamma (= 5/3)$ being the adiabatic index, so that a simple ideal gas with a constant specific heat ratio is assumed. While n_s is the number density, \mathbf{v}_s is the velocity, p_s is the scalar pressure, and T_s is the temperature for the particle species s , either an i or e in the appropriate equation; \mathbf{E} is the electric field, $\mathbf{B} (= \hat{\mathbf{y}} \times \nabla \psi + B_y \hat{\mathbf{y}})$ is the magnetic field, \mathbf{g} is the gravitational acceleration, ψ is the flux function, k_B is Boltzmann's constant, and $\bar{\mathbf{I}}$ is the identity matrix. The variables \tilde{p}_e and \tilde{n}_e represent the perturbed electron pressure and density, respectively, compared to their initial values and are explained in the following subsection. All physical quantities in this paragraph are represented in non-dimensionalized form by the following proper normalization scheme.

While an MHD normalization has no intrinsic length or time scale, a two-fluid normalization does not have the freedom of choice. In the normalization scheme adopted for this study, the length and time scales are normalized respectively by the ion inertial length, d_i , and the inverse of the ion cyclotron frequency, $1/\omega_{ci}$. Therefore, the adopted full normalization scheme becomes:

$$\begin{aligned} (x, z) &\rightarrow (x, z)/d_i; & t &\rightarrow t\omega_{ci}; \\ (\mathbf{v}_i, \mathbf{v}_e) &\rightarrow (\mathbf{v}_i, \mathbf{v}_e)/v_0; & (n_i, n_e) &\rightarrow (n_i, n_e)/n_0; \\ k_b &\rightarrow k_b/(B_0^2/4\pi n_0 T_0); & (T_i, T_e) &\rightarrow (T_i, T_e)/T_0; \\ (p_i, p_e) &\rightarrow (p_i, p_e)/(B_0^2/4\pi); & \mathbf{B} &\rightarrow \mathbf{B}/B_0; \\ \mathbf{E} &\rightarrow \mathbf{E}/(B_0 v_0/c); & \psi &\rightarrow \psi/(d_i B_0); \\ \mathbf{g} &\rightarrow \mathbf{g}/(v_0^2/d_i), \end{aligned}$$

where $d_i = c/\omega_{pi}$ is the ion inertial length, $\omega_{pi} = \sqrt{4\pi n_0 e^2/m_i}$ is the ion plasma frequency, $\omega_{ci} =$

$|e|B_0/m_i c$ is the ion cyclotron frequency, and $v_0 = B_0/\sqrt{4\pi n_0 m_i}$ is the Alfvén speed at the base. This normalization introduces two ratios into the governing equations, namely, the ion mass to electron mass ratio, m_i/m_e , and the speed of light to the base Alfvén speed ratio, c/v_0 . Unless otherwise stated, the adopted values for these ratios are $m_i/m_e = 25$ and $c/v_0 = 10$.

In the true solar corona, the ion inertial length d_i is many orders of magnitude smaller compared to the global length scale of large magnetic structures that occupy the corona. The length scale adopted by Choe & Lee (1996a,b) is $L_0^{CL} = 3.0 \times 10^9$ cm which in their MHD simulations represents the half-distance between B_z (B_y in their geometry) extrema of the magnetic arcade at the base. It is impossible practically to run a simulation currently with enough grid points that is able to resolve the real amount of ion inertial lengths contained within the global length scale of the magnetic arcade itself. Therefore, the two-fluid simulations in this paper whose length scale is normalized to d_i can at best produce qualitative results by assuming an artificially large d_i . Simultaneously, we must also ensure that the ion inertial length is still much smaller than the global length scale of the arcade l_0 simulated, i.e., $l_0 = 2L_0^{CL} \gg d_i$, so that important two-fluid effects can still be resolved within the structure of the arcade. We conducted several simulations with varying values of d_i as fractions of L_0^{CL} for the purpose of a convergent study. The adopted values for d_i investigated were $d_i/L_0^{CL} = 1/5, 1/10, 1/20$, and $1/30$ while the grid resolution within one d_i length span remained the same. We observed nearly identical behavior across simulations performed in the convergent study, the results of which are detailed in §3.2. Therefore we feel confident that artificially increasing d_i has a minimum effect of the qualitative behavior of the arcade evolution as long as $l_0 \gg d_i$.

We use the same values for the normalizing constants n_0 , v_0 , and B_0 as those used in Choe & Lee (1996a,b). The magnetic field \mathbf{B} is normalized by $B_0 = 50$ G representing the maximum magnitude of B_z at the base. The ion and electron number densities are both normalized by $n_0 = 1.0 \times 10^9$ cm $^{-3}$ which is the assumed proton number density at the photosphere. The bulk velocities, \mathbf{v}_i and \mathbf{v}_e , are both normalized by $v_0 = 3.4 \times 10^8$ cm s $^{-1}$ representing the Alfvén speed at the base. While the ion and electron temperatures, T_i and T_e , are both normalized by $T_0 = 2.0 \times 10^6$ K. The gravitational acceleration $\mathbf{g} = -g(z)\hat{\mathbf{z}}$ is a function of the vertical coordinate z taking the form

$$g(z) = \frac{4\pi G M_\odot}{(R_\odot + z)^2} = g_0 \frac{R_\odot^2}{(R_\odot + z)^2}, \quad (12)$$

where G is the gravitational constant, M_\odot is the solar mass, R_\odot is the solar radius, and $g_0 = 2.7 \times 10^4$ cm s $^{-2}$ is the surface gravity of the Sun. Finally, \mathbf{g} is then normalized by v_0^2/d_i .

Numerical studies of coronal magnetic arcade shearing usually prescribe symmetrical initial conditions and boundary conditions for all physical variables, especially for the magnetic arcade and the imposed shearing profile. In a MHD study of magnetic arcade shearing, it is only necessary to simulate the half of the domain on one side of the magnetic neutral line ($x = 0$), since the plasma’s motions will be symmetric about this line. However, in a two-fluid simulation consisting of charged particles with different masses, symmetric motions of the ions and electrons are not guaranteed across the magnetic and shearing neutral line due to symmetry breaking of the static electric field. With this being the case, the computational domain employed in the study consists of the entire corona on both sides of the neutral line. We employ a square computational domain $\{(x, z) | -80\alpha \leq x \leq +80\alpha, 0 \leq z \leq +160\alpha\}$ with a uniform gridding consisting of $(240\alpha + 5) \times (240\alpha + 5)$ mesh points, where $\alpha \equiv L_0^{CL}/d_i$ is the length scaling ratio between the normalized d_i and the fixed length scale used by Choe & Lee (1996a). The governing equations are solved to fourth-order accuracy in both space and time using a 5-point central differencing and fourth-order Runge-Kutta integration algorithm. This explicit scheme ensures that the transmission of information throughout the computational domain at all characteristic wave speeds is included in the numerical solutions.

2.2. Initial and Boundary Conditions

The simplest initial state of the plasma assumes charge neutrality and hydrostatic equilibrium within the solar corona. From the governing equations, these conditions take the form $\nabla p_i = n_i \mathbf{g}$, $\nabla p_e = \frac{m_e}{m_i} n_e \mathbf{g}$, $n_i(z, t = 0) = n_e(z, t = 0) = n^{t=0}(z)$, $\mathbf{v}_i = 0$, and $\mathbf{v}_e = 0$. Since the overwhelming majority of mass that must be supported against gravity comes from the ion fluid, the initial density profile of both the ions and electrons is derived from the hydrostatic equilibrium equation for ions, i.e., $\nabla p_i = n_i \mathbf{g}$. The densities are derived while assuming that the initial temperature profiles of both the electrons and ions are both uniform in space with the initial ion temperature set to $T_i = 2.0 \times 10^6$ K and the initial electron value set to half that value, $T_e = 1.0 \times 10^6$ K. This produces the same initial density profile employed by Choe & Lee (1996a). We assume a slightly lower value for the initial electron temperature from observations (Landi 2007). Unless we chose an unrealistically low initial electron thermal tempera-

ture, the magnitude of the initial electron pressure force derived from the ion density profile is greater than the magnitude of the gravitational force. To satisfy the initial equilibrium in the electron momentum equation, the pressure and gravitational terms are replaced with $\frac{m_i}{m_e} \nabla p_e \rightarrow \frac{m_i}{m_e} \nabla \tilde{p}_e$ and $n_e \mathbf{g} \rightarrow \tilde{n}_e \mathbf{g}$, respectively, where $\tilde{p}_e = p_e - p_e^{t=0}$ and $\tilde{n}_e = n_e - n_e^{t=0}$, therefore the accented quantities represent the perturbed values from the initial equilibrium values. This setting gives the freedom to select any electron temperature while still maintaining charge neutrality.

The initial state of the fields are assumed to be force-free with the initial electric field set to $\mathbf{E} = 0$ while the initial flux function is chosen to produce a purely potential magnetic field, i.e., $\nabla^2 \psi = 0$, with no initial toroidal magnetic component B_y . We use the same potential dipole flux profile as Choe & Lee (1996a) but transformed into our scaling depending on the adopted value of d_i . The initial normalized potential profile becomes

$$\psi(x, z, t = 0) = \frac{8\alpha^2}{\sqrt{3}} \frac{(z + \alpha\sqrt{3})}{x^2 + (z + \alpha\sqrt{3})^2}, \quad (13)$$

where $\alpha \equiv L_0^C/d_i$. From this flux profile, the maximum strength of the normal magnetic field at the bottom boundary, $|B_z|$, is located at $x = \pm\alpha$, matching the same dimensional length span as Choe & Lee (1996a) and is equal to unity, corresponding to the value $B_0 = 50$ G. The initial magnetic and pressure profiles produce a plasma beta of $\beta = P_{tot}/(B^2/2) = 4.2 \times 10^{-3}$ at the base. We also note as Choe & Lee (1996a) has that without gravity the plasma β would become too large in the upper regions of the domain to satisfy a low- β corona.

The Runge-Kutta integration requires that the time variation of variables be extraneously specified at the boundaries. For simplicity, the upper boundary and the two lateral boundaries are approximated by a zeroth-order extrapolation for all incremental time variations of the variables except ψ (and therefore B_x and B_z). Analytically, this takes the form

$$\frac{\partial(\Delta\phi_i)^t}{\partial x_\perp} = 0, \quad (14)$$

where ϕ_i represents all variables at both the two lateral boundaries and the top boundary (excluding ψ , B_x , and B_z), x_\perp is the coordinate variable normal to the particular boundary, and $(\Delta\phi_i)^t$ is the incremental time variation of ϕ_i at each time step. While the flux function is updated at the boundaries using the governing equation $\partial\psi/\partial t = E_y$.

At the bottom boundary, we also use the same shearing profile employed by Choe & Lee (1996a), except

transformed into our length scale, and apply it to both the ions and the electrons. The normalized shearing profile is given by

$$v_{iy}(x, z = 0, t) = v_{ey}(x, z = 0, t) = f_y(t)V_y(x), \quad (15)$$

where

$$V_y(x) = \frac{1}{\alpha} V_{y0} x \exp\left[\frac{1}{2} - \frac{1}{2}\left(\frac{x}{\alpha}\right)^2\right] \quad (16)$$

and

$$f_y(t) = \begin{cases} t/t_r & \text{if } 0 \leq t \leq t_r; \\ 1 & t_r \leq t. \end{cases} \quad (17)$$

This shear velocity profile is antiparallel across the neutral line ($x = z = 0$) and is linearly increased from zero to its full value in $t_r = 60\alpha$. Also it is worth noting that the shear velocity extrema are located at the normal magnetic field extrema at the base. This profile is used for all cases in this study.

No converging flow is assumed in the current simulation and the x -components of the ion and electron velocities are set to zero, i.e., $v_{ix} = v_{ex} = 0$. In the denser photosphere, we assume that the heavier ions are constrained to have no vertical motions at the boundary ($v_{iz} = 0$), while the lighter, more mobile, electrons are allowed to exercise vertical motion under the free boundary condition given above. This free boundary on the electron's vertical motions is assumed out of necessity since it seems to suppress unphysical waves in the electric field that would otherwise emanate from the bottom boundary into the computational domain. The time evolution of the ion energy is determined based on the time derivative of this shearing flow while assuming that the ion pressure in the boundary layer remains unchanged. The free boundary condition is applied to the electron energy, matching its vertical motion condition. The densities, n_i and n_e , are set to be constant in time and equal to the initial value n_0 . The shearing motion imposed at the bottom causes the fluid elements to move a distance

$$\zeta(x, t) \equiv \int_0^t f_y(t')V_y(x, t')dt', \quad (18)$$

after a time t . Since the ion and electron motions are synchronized at the bottom boundary and assuming an ideal, non-resistive plasma, it holds that the arcade footpoints move tightly with the fluid elements, therefore the half-distance between two conjugate footpoints, Y , obeys $|\zeta| = |Y|$. While the maximum shear obtained at time t is

$$\zeta_m(x, t) = V_{y0} \int_0^t f_y(t')dt'. \quad (19)$$

Sketches of the initial system and the motions due to the shearing profile can be seen in Figure 1.

The electric field components are updated based on the ideal Ohm's law, $\mathbf{E} + \mathbf{v}_e \times \mathbf{B} = 0$, derived from the electron momentum equation and taking the limit as $m_e \rightarrow 0$ and ignoring Hall and diamagnetic terms. The horizontal and normal electric fields, E_x and E_z , are updated directly at every time step by substituting the shear velocity, v_{ey} , and v_{ez} into the ideal Ohm's law. Despite the electrons performing vertical motions, we tactically assume that E_y remains zero at the base; corresponding to this condition, ψ remains unchanged in time. With unchanged ψ at the bottom boundary, B_z also remains unchanged in time. This constraint is consistent with observations since the normal component of the photospheric magnetic field remains constant during eruptive events, like CMEs and flares (Forbes 2000).

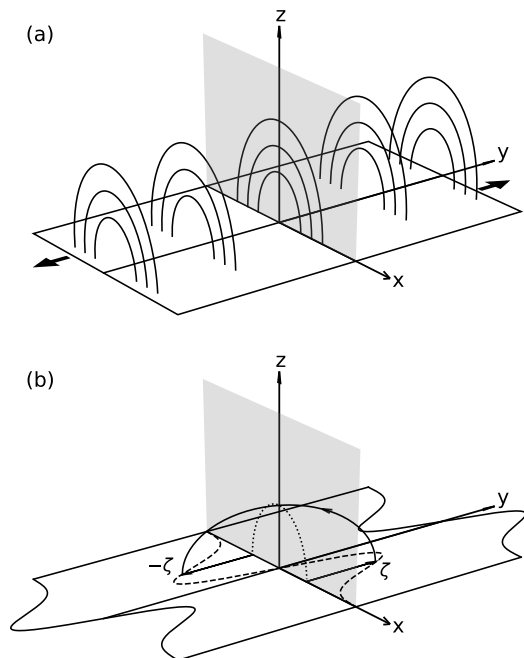


Figure 1. The sketch (a) represents the initial system of a magnetic arcade that is homogenous along the magnetic neutral line collinear with the y -axis. The schematic (b) illustrates a single arcade field line before (dotted curve) and after (solid curve) its conjugate footpoints have moved each a distance $|Y| = |z|$ from the x -axis, where z is the shearing distance of the photospheric fluid elements. In the x - y plane, the large black arrows (a) reference the direction of shearing on each side of the neutral line and the dashed curve (b) represents the shearing profile of the arcade footpoints. The gray opaque box co-planar to the x - z plane represents the computational domain of the simulation. Note that the shearing profile has been enlarged for clarity.

The B_x component is updated using one-sided differencing of $\partial^2 B_x / \partial z^2 = 0$ at the bottom boundary since it produces more stable results than updating B_x by its governing equation.

The sheared magnetic arcade is described by the profile of the its toroidal magnetic field, B_y , which significantly affects the global evolution of the arcade. The best method to update B_y may be to apply a field line tracing algorithm that traces a field line from its footpoint moving distance, Y , up to the vertical plane ($x = 0$) and incrementally changing its value depending on whether the field line passes through the plane prematurely or otherwise as in MHD simulations by Steinolfson (1991). Perhaps owing to the fact that the horizontal and normal electric fields are updated directly from the known shear profile, quality numerical results are obtained for B_y by merely using one-sided differencing of $\partial B_y / \partial z = 0$ at the bottom boundary.

3. NUMERICAL RESULTS AND DISCUSSION

In this section, numerical results based on the ideal two-fluid model described in the preceding section are presented and discussed. In the first subsection, we present the results of a representative case that exhibits characteristics and features that are seen to be qualitatively general across broad regimes of four different parameters for simulations undertaken. In the second subsection, results from parameter studies are presented and their results discussed in relation to the representative case. For the representative case and the first three parameter studies, we adopt the normalized value for the ion inertial length as $d_i / L_0^{CL} = 1/5$.

3.1. Representative Case

The remaining parameter to be selected is the maximum shear speed at the base, V_{y0} . In Choe & Lee (1996a), they performed simulation runs using two different shear speeds, $0.01v_0$ and $0.001v_0$, which corresponds to the dimensional speeds 34 km s^{-1} and 3.4 km s^{-1} , respectively. For the representative case in this subsection, we selected the intermediate value $V_{y0} = 0.005v_0$; in addition, a simple parameter study for the maximum shear velocity is undertaken and its effects on the simulation results are summarized in the following subsection.

Figure 2a shows a magnified view of the initial dipole magnetic field and the initial density profile where the red dashed line represents the polarity line ($x = y = 0$) of the arcade collinear with the z -axis. The representative case simulates up to a maximum shear of $\zeta_m = 31.00d_i (= 6.2L_0^{LC})$ and the evolution of the field configuration remains very similar to that observed in

Choe & Lee (1996a). Figures 2b and 2c exhibit the magnetic field (black lines) superimposed on color density plots of the toroidal electron current density, $-J_{ey}$.

Initially, the magnetic topology evolves in a self-similar fashion as the entire arcade undergoes an outward expansion. At $\zeta_m \gtrsim 20d_i$, the self-similar expansion of the magnetic field ceases as it begins to acquire stronger vertical motions in the central region with the inner field lines becoming stretched vertically and pinched laterally above the points of maximum normal magnetic field, $|B_z|$, and maximum shear velocity reversing the local field curvature vectors. Consequently, the toroidal electron current density $-J_{ey}$ also pinches and migrates upwards along the polarity line and is indicative of the first stages of a growing current layer with finite width at the central region of the arcade. With the ever-growing arcade footpoint shearing, the feet of the electron current layer remain bifurcated at the base. Choe & Lee (1996a) categorize a current layer for their simulations at a maximum shear of $\zeta_m \sim 35d_i$ in our length scale. In their second paper, Choe & Lee (1996b), $\zeta_m = 30d_i$ is found to be a critical value for which any smaller value of shear does not produce magnetic reconnection in the strong current layer region regardless of resistivity strength. It is also evident that the electron motions strongly flow along the field lines. Comparatively, the motions of the ions (not shown) are more complicated and exhibit anti-symmetric behavior about the polarity line. The strongly line-tied motion of the electrons that is observed is taken as evidence that the current gridding is sufficient enough to resolve both the different ion and electron motions separately despite having inadequate resolution for the electron skin depth, $d_e/d_i = \sqrt{m_e/m_i}$.

Beyond the confines of the inner field and current layer regions, a conspicuous difference in the two-fluid simulations emerges compared to the MHD studies mentioned previously. The difference manifests as a strengthening wave that evolves into a shock that separates the outwardly flowing plasma and the unperturbed plasma. Figure 3 shows the vertical ion velocity for different values of ζ_m . This is where the current study diverges from the simulations by Choe & Lee (1996a). In the early stage as shown in Figure 3a, there is no noticeable formed discontinuity. At $\zeta_m = 18d_i$ (see Fig. 3b), a discernible arching discontinuity is clearly visible in the front of the outflow with the maximum speeds of the ions, electrons, and discontinuity all exceeding the local ion sound and Alfvén speeds, $V_S^i = \sqrt{\gamma k_b T_i}$ and $V_A^i = B/\sqrt{n_i}$, as viewed in the rest frame. Finally, in Figure 3c, the strength of the discontinuity in the vertical ion velocity has saturated to its maximum value

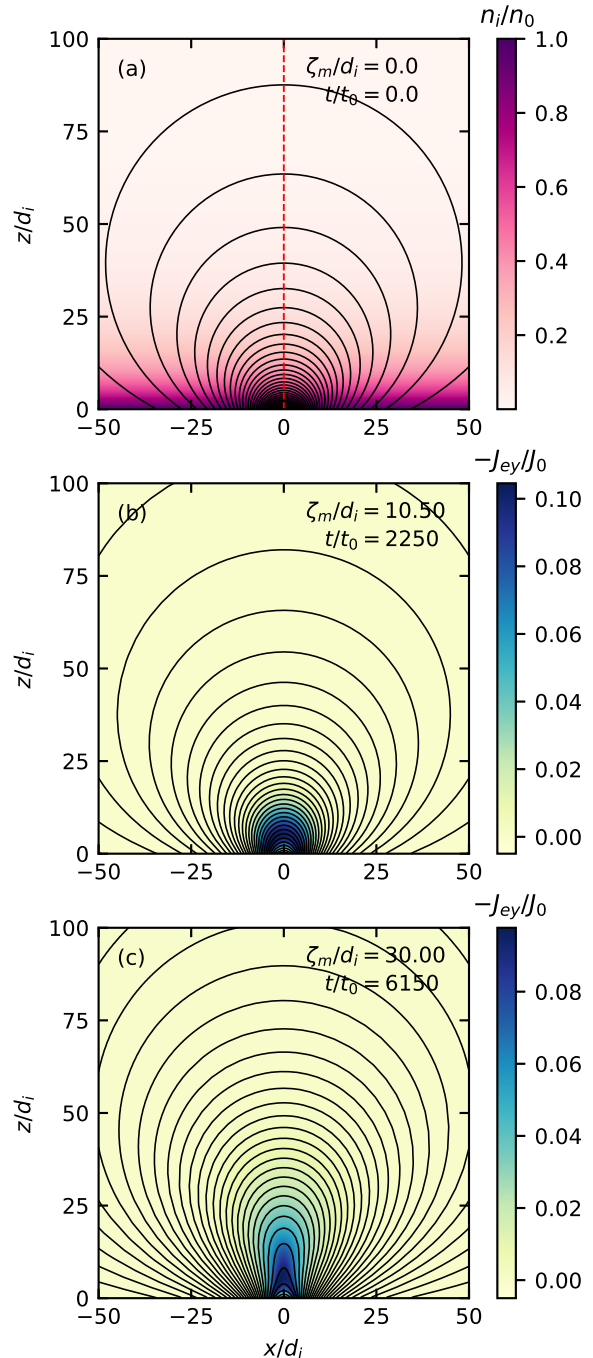


Figure 2. (a) Initial potential magnetic field profile (black lines) superimposed on a color contour plot of the initial electron and ion density profiles, where the polarity line is referenced by the dashed red line and is collinear with the z -axis. (b) and (c) are snapshots of the magnetic field (black lines) and the toroidal electron current density $-J_{ey}$ for different values of the maximum shear ζ_m .

for the entire simulation and the upstream and downstream regions are clearly separated. The black curve

is a single magnetic field line and is plotted to illustrate that the discontinuity motions are very nearly perpendicular to the local magnetic field, especially above the neutral line. The local electron sound speed and Alfvén speed are much faster compared to the ion’s characteristic speeds, since the ratio between them is dependent on the mass ratio m_i/m_e whose normalized quantities are defined as $V_S^e \equiv (m_i/m_e)^{1/2} \sqrt{\gamma k_b T_e}$ and $V_A^e \equiv (m_i/m_e)^{1/2} B / \sqrt{n_e}$. Despite the electron motions always remaining sub-sonic and sub-Alfvénic, the discontinuities still form.

In order to classify the propagating discontinuity, we perform “in-situ”-like observations of the various physical quantities (see Fig. 4) as the discontinuity passes through the point $(0, 675)$ directly above the origin after the ion fluid velocity begins propagating beyond its local sound and Alfvén speeds in the rest frame. The physical quantities are continuously recorded at this specific reference point because it is easier to analyze their time variations and differentiate between the upstream and downstream behaviors. The analysis would become cumbersome if snapshots of the variable profiles were recorded instead since the initial magnetic and density profiles are highly nonuniform. This location for performing the in-situ observations is chosen since the discontinuity rotation angle, the angle between the normal direction of the discontinuity surface and the z -axis, is $\theta_R = 0^\circ$ thereby simplifying the analysis; meanwhile the discontinuity normal angle, $\theta_N = |\arctan(B_T/B_N)|$, is approximately 90° since $B_T \gg B_N$ corresponding to a perpendicular discontinuity, where B_T and B_N refer to the tangential and normal magnetic fields with respect to the discontinuity surface, respectively. Note that the physical quantities in Figure 4 are all observed in the rest frame.

For the duration of the observations taken in Figure 4, the average propagation speed of the discontinuity along the polarity line is observed to be $v_p = 0.113v_0$. We introduce the curly bracket $\{\phi\} = \phi_D - \phi_U$ to denote the jump of a variable ϕ between the upstream (subscript U) and downstream (subscript D) regions. Typically, one would analyze the jumps by transforming into the de Hoffmann-Teller frame (de Hoffman & Teller 1950), however this frame of reference does not exist for purely perpendicular discontinuities. Therefore, the analysis is performed by transforming into the normal incidence frame of the discontinuity, which is the frame of reference that is co-moving with the discontinuity surface normal collinear with the z -axis. After transforming into this frame of reference, it is evident at the discontinuity that $\{n_i\} \neq 0$, $\{n_e\} \neq 0$, $\mathbf{v}_i^N \neq 0$, and $\mathbf{v}_e^N \neq 0$, where \mathbf{v}_i^N and \mathbf{v}_e^N are the ion and electron ve-

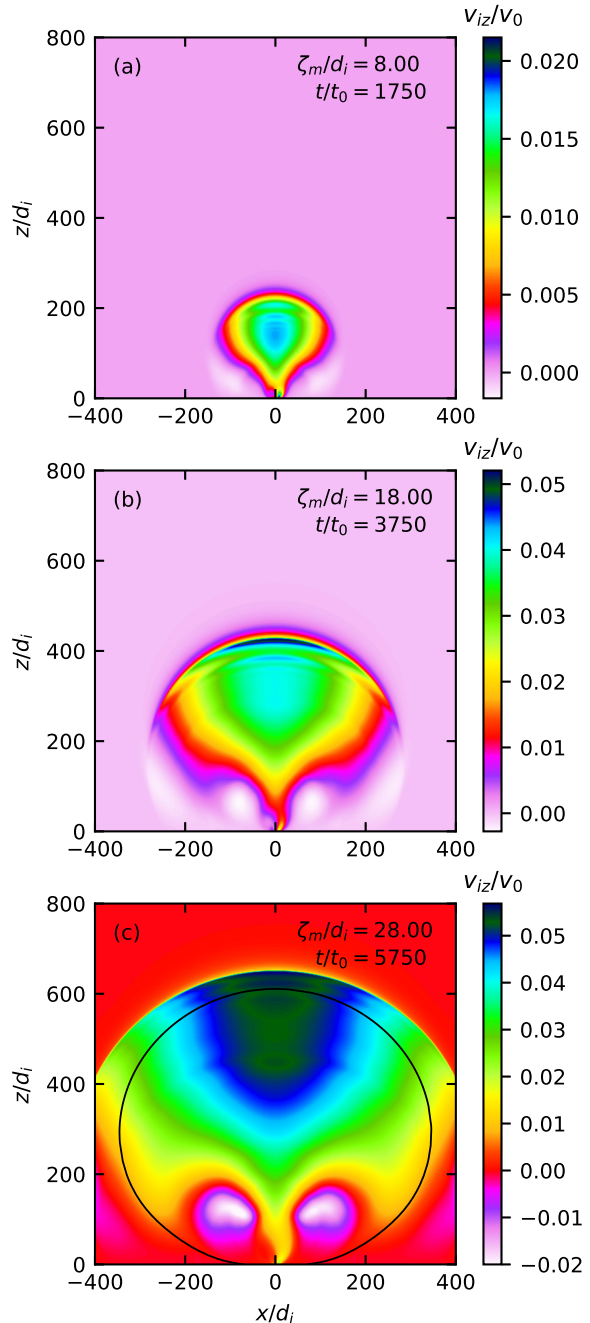


Figure 3. The evolution of the discontinuity in the ion’s vertical motions. A snapshot of the pre-shock formation stage is seen in (a), by (b) a discernible strong MHD fast-like shock has formed, and finally by (c) the shock strength has peaked to its maximum value for the simulation.

locities normal to the discontinuity surface, respectively. Consequently, the discontinuities seen in this study do not correspond to either contact, rotational, nor tangential discontinuities but are consistent with shocks, since shocks are classified by both fluid velocity and a density

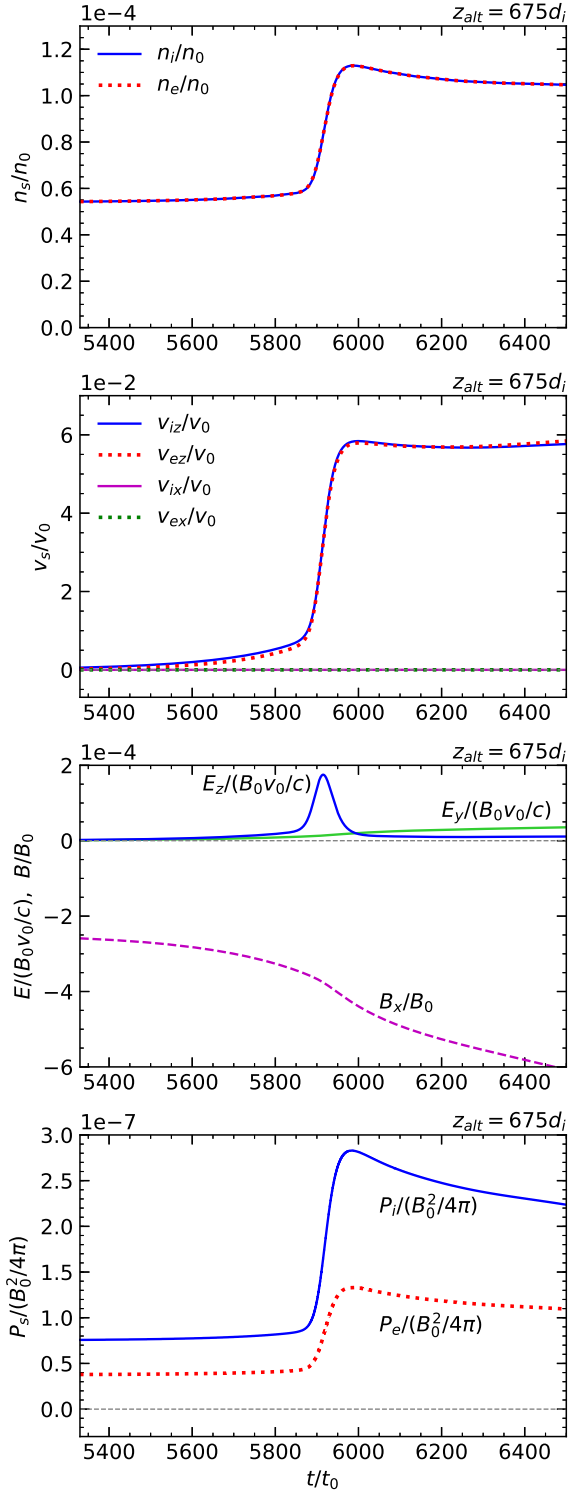


Figure 4. Pertinent plasma and field values continuously observed at $z_{alt} = 675d_i$ versus time with the discontinuity passing through this altitude at approximately $t = 5960t_0$. The upstream and downstream regions are easily distinguishable.

jump, i.e., compression, across the discontinuity surface. This frame co-moving with the discontinuity will now be referred to as the shock frame.

Shocks and discontinuities are analyzed based on jump conditions obtained from conservation laws. In MHD theory, the shock jump conditions are defined by the MHD Rankine-Hugoniot relations, while analogous jump conditions have also been derived for theories of two-fluid plasmas in certain limits by both [Sen & Spero \(1967\)](#) and [Woods \(1969\)](#). We adopt jump conditions modified from our governing equations in the perpendicular limit as $\theta_N = |\arctan(B_T/B_N)| \approx 90^\circ$, since $B_N \approx 0$. The pertinent jump conditions are

$$\{n_i v_i^N\} = 0, \quad (20)$$

$$\{n_e v_e^N\} = 0, \quad (21)$$

$$\{n_i (v_i^N)^2 + P_{tot} + \frac{B_T^2}{2}\} = 0, \quad (22)$$

$$\{E_T\} = \{\mathbf{v}_e^N \times \mathbf{B}_T\} = 0, \quad (23)$$

where P_{tot} is the sum of the ion and electron pressures. Equation (22) is derived by the usual limiting pillbox volume integration of the sum of the ion and electron momentum equations across the discontinuity after first multiplying the electron momentum equation with the ratio m_e/m_i and then taking the limit $m_e/m_i \rightarrow 0$. All gravity terms are ignored.

To compare the numerical results observed in this simulation to the theoretical values predicted by the jump conditions, we define the errors between the numerical results and theoretical results as $|\phi_D - \phi_*|/|\phi_D|$, where ϕ_D represents the numerical downstream value of a particular variable and ϕ_* is the downstream fitted value calculated purely from the upstream quantities based on the jump conditions. It should be noted that only the coplanar variables are analyzed, i.e., x - and z -component variables that are in the simulation plane. The results of the analysis are tabulated in Table 1 and it is evident that the observed downstream quantities fit fairly close to their predicted values. Meanwhile, the downstream and upstream values of v_i^T , v_e^T , E_T , and B_N do vary across the shock. However, their magnitudes and variances remain many order of magnitudes smaller than the pertinent variables for a perpendicular shock easily satisfying $(v_i^T, v_e^T, E_T, B_N) \ll (v_i^N, v_e^N, E_N, B_T)$, therefore we feel confident ignoring these discrepancies. Also, these discrepancies and the errors in the observed and theoretical values could be contributed to the fact that the observed shock is not a planar, zero-width,

Table 1. The upstream and downstream values observed in Figure 4 calculated in the shock frame with the downstream fitted values calculated from the upstream quantities based on the jump conditions.

	Upstream	Downstream	Fitting	Error
n_i (10^{-4})	0.555	1.08	1.12	3.7%
n_e (10^{-4})	0.555	1.08	1.13	4.6%
v_i^N	-0.113	-0.056	-0.058	3.6%
v_e^N	-0.113	-0.053	-0.058	9.4%
B_T (10^{-4})	-2.95	-5.25	-5.74	9.3%
P_{tot} (10^{-7})	1.15	3.61	3.90	8.0%

steady-state discontinuity assumed in the theoretical model. In our simulations, the shock has a finite width and is not stationary nor in steady-state, but constantly propagating in an initially nonuniform magneto-plasma.

In the shock frame, the flow speed into the shock from the upstream is greater than the flow speed out of the shock into the downstream; this is clear from Table 1. Viewed in the rest frame, the shock wave is propagating faster than both the upstream and downstream velocities. Regardless of which frame the shock is viewed, there is always flow across the shock. This shock wave observed in Figure 4 is propagating well beyond the upstream ion sound and ion Alfvén speeds with respective Mach numbers clocked at $M_S = 2.35$ and $M_A = 3.32$, where a Mach number refers to the ratio of the upstream flow into the shock versus a particular upstream characteristic speed as viewed in the shock frame. In the perspective of MHD, perpendicular shocks only produce fast mode shocks. In the perpendicular limit, the MHD fast mode phase velocity becomes $v_{fm} = \sqrt{V_S^2 + V_A^2}$ and takes on the value $v_{fm} = 0.061v_0$ at $z = 675d_i$, where we are assuming that V_S and V_A refer to the local ion sound and Alfvén speeds, respectively. Viewed from the shock frame, it is clear that both the ion and electron upstream velocities exceed v_{fm} or, equivalently, viewed in the rest frame the shock wave is propagating beyond v_{fm} . Finally, since there is compression and fluid flow across the discontinuity surface, the jump conditions are adequately satisfied, and $v_p > v_{fm}$, we conclude that the discontinuity observed is a propagating fast-like shock driven by the motions at the base.

We begin analyzing the forces acting on the expanding wavefront at $\zeta_m = 5.0$ since for earlier times the wave has not reached a sufficient altitude for it to be easily distinguished from the stronger plasma motions near the base. Evidently from Figure 5, the forces acting on both the electron (see Fig. 5a) and ion (see Fig. 5b) fluids that propels the strengthening of the wave into a shock are quite different.

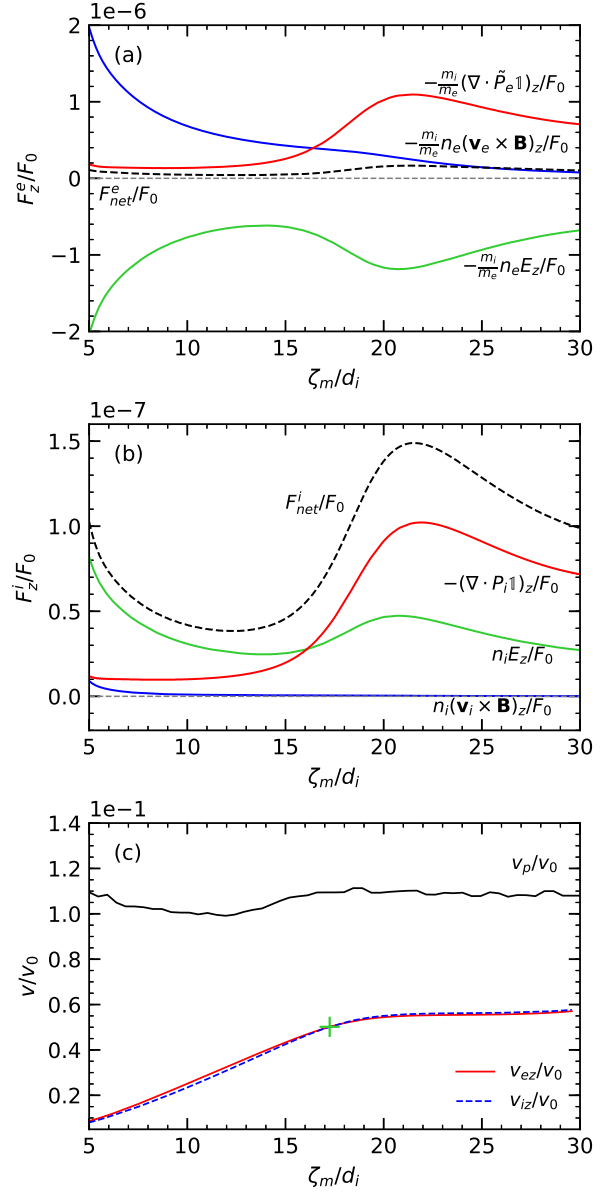


Figure 5. Plots of the extrema values of the forces acting on the electrons (a) and ions (b) measured at the wavefront as a function of maximum shear ζ_m . Gravity is not plotted due to its minimal effect as the wavefront moves to higher altitudes. The net forces (black dashed lines) are also plotted. Plot (c) shows the maximum values of the ion and electron vertical velocities as viewed in the rest frame where the green + is the point where the ion vertical velocity exceeds the electron's vertical velocity; while the black curve is the vertical propagation velocity of the wave calculated from numerical derivative of the wavefront's position.

Initially the electrons are mainly accelerated upwards by the magnetic pressure from the $n_e(\mathbf{v}_e \times \mathbf{B})$ Lorentz term while the net thermal pressure provides a smaller fraction of the upward acceleration. Meanwhile, the

magnetic pressure force experienced by ions is nearly two orders of magnitude smaller. The lighter electrons being line-tied move tightly with the expanding arcade propelled by the magnetic pressure, while the heavier ions do not move directly with the arcade and show signs of slight slippage. This difference in motion as the electrons slip past the slower ions in a stratified atmosphere produces a growing charge separation that gives rise to a locally strong electric field. Snapshots of the charge separation in the pre- and post-shock formation stages can be seen by the profiles of the net charge $(n_i - n_e)/n_0$ along the polarity line (z -axis) for three different values of ζ_m in Figure 6. The discontinuity wavefront is strongly saturated by electrons followed by the lagging ions below and this behavior is seen at all times in the simulation. This alternating electron and ion rich regions gives rise to nonlinear behavior in the net charge further below. As this charge separation in the electrons and ions grows, so too does the local electric field and it is this electric field that provides the bulk of the upward acceleration of the ions in this shock formation stage and acts as a moderating force against the electrons.

The propagation speed of the growing discontinuity wave exits the inner arcade at $v_p = 0.136v_0$ and gradually decelerates approximately to $v_p = 0.100v_0$ before accelerating to a steady value averaged at $v_p = 0.113v_0$ for the rest of the simulation. The initial local Alfvén velocity decreases with increasing altitude while the initial sound speed is uniform throughout the computational domain due to the assumed uniform initial temperature. Therefore, as the wave propagates into higher

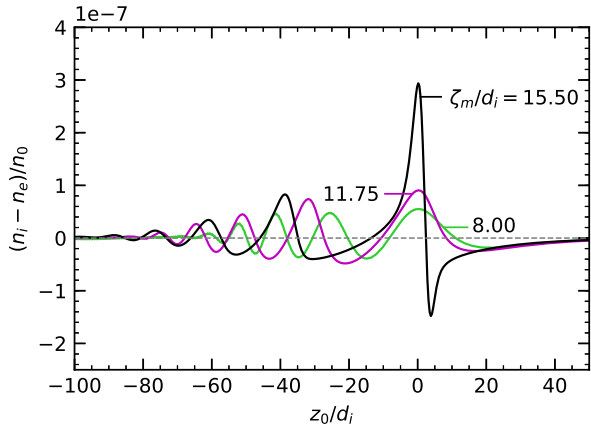


Figure 6. Superimposed net charge density profiles for three different values of maximum shear ζ_m along the polarity line. The superposition is aligned by the point z_0 which corresponds to the altitude of the maximum net charge at the discontinuity for that particular value of ζ_m . It is clear that the discontinuity is always preceded by a greater saturation of electrons.

regions of the corona, its velocity simultaneously reaches to and then eventually surpasses the phase velocity of the MHD fast mode. For this simulation, the discontinuity wave is observed surpassing v_{fw} at $\zeta_m = 9.8d_i$ where in dimensional units the characteristic speeds at the discontinuity locale are $V_S^i = 165 \text{ km s}^{-1}$ and $V_A^i = 289 \text{ km s}^{-1}$ with the discontinuity propagation speed clocked at $v_p = 332 \text{ km s}^{-1}$ at an altitude of $z = 240d_i$. The wave is now classified as a propagating fast-like shock.

The shock wave continues to strengthen as it propagates into an increasingly tenuous plasma. By $\zeta_m \approx 15d_i$, the local electron and thermal pressures become the forces providing the bulk of the upward acceleration as the shock begins to strongly ram the unperturbed plasma in the upstream region. As the shock propagates into higher altitudes, the thermal pressure forces strengthen as it rams into the tenuous plasma. The local upward ion speed surpasses the local upward electron speed for the first time at $\zeta_m = 17.4d_i$ (see Fig. 5c). This point corresponds to an inflection point where the strengthening of the electric field begins to decelerate. Then, the ions in the downstream in the wake of the shock reach super-Alfvénic speeds at $\zeta_m = 19d_i$ as viewed in the rest frame, where shortly afterward the electric forces acting on the ions and electrons reach their extrema values for the entire simulation. The weakened electric field also weakens the ramming against the unperturbed plasma and the thermal pressure also reaches a maximum subsequently.

Finally, for $\zeta_m > 20d_i$, the shock propagation speed is no longer accelerating and the electric and thermal pressure forces have reached their extrema values for the entire simulation. Afterward, their absolute magnitudes begin to saturate to reduced values, however, the shock strength continues to increase slightly as the shock carries on propagating through the increasingly tenuous atmosphere.

The shock and the expanding arcade affect the thermodynamic evolution of the system. The global ion temperature profiles in the simulation plane are recorded in Figure 7a and 7c for $\zeta_m = 11.25d_i$ (a) and $\zeta_m = 24.00d_i$ (c), respectively, and are ratioed to the initial ion temperature, T_{i0} . The electron temperature profile is quantitatively similar, except in the very low regions of the arcade where the electrons experience greater heating. Above this lowest region of the arcade, there are two distinct zones similar for both the ion and electron fluids. The first zone (solid line contours) corresponds to heating by the shock as it rams and then passes through the initially stationary plasma. For a perpendicular shock, like the one seen in this simulation, the shock propagates across the magnetic field lines and compresses both the

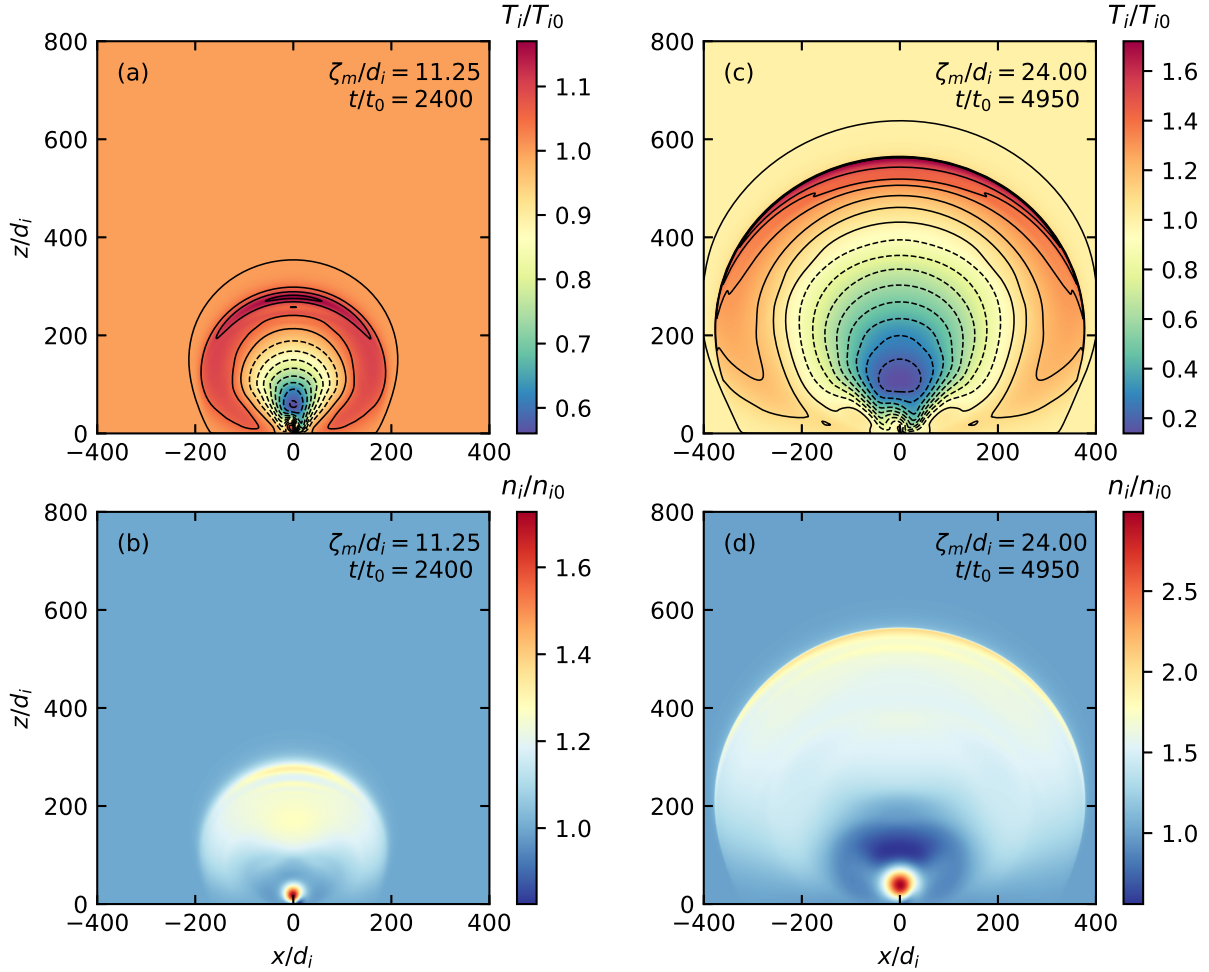


Figure 7. The ion temperature profiles (a, c) with corresponding contour lines and the ion density profiles (b, d) for $\zeta_m = 11.25d_i$ and $\zeta_m = 24.00d_i$ ratioed to the initial ion temperature and density profiles, respectively. For the temperature plots, solid contour lines demarcate the heated zone and dashed contour lines demarcate the cooled zone. The ions and electrons both experience strong heating and compression at the shock surface.

plasma and the magnetic field, hence the coupled dependence on both V_S and V_A . It is clear that around the lip of the shock in Figure 7b and 7d that the ion density ratio reaches a local maximum corresponding to this compression. For strong shocks, the compression in the transition region is so abrupt that the system cannot be considered in a succession of equilibrium states but refers to an irreversible process, i.e., an increase in entropy, with dissipation of energy in the form of heating (Sears 1953). The maximum heating seen at the shock in Figure 7c corresponds to an approximate increase of the ion temperature in real terms by 1.4 million Kelvin. At first glance it might appear that this observed shock could provide an explanation for the coronal heating problem, since this global heating and the expanding shock are produced merely by closed field lines shuffling at the photosphere which occurs regularly on the sun.

Yet, the heating is eventually extinguished by the second zone (dashed line contours) which trails the first and represents an inflating zone of cooling. This decrease in temperature is also seen in simulations by Steinolfson (1991) where the adiabatic cooling is generated by the rapid expansion of the magnetic arcade and the plasma in the lower portions of the arcade.

Lastly, it is worth commenting on the local ion and electron heating at the shock (see Fig. 8). Initially, the heating experienced by the electrons is only slightly greater than that experienced by the ions. However, at $\zeta_m = 18d_i$ and right after the vertical ion velocity exceeds the electron vertical velocity, the two heating ratios begin to diverge in favor of the ions. This preferential heating of the ions results in a 6.7% greater heating ratio compared to the electrons with respect to their initial temperatures by the end of the simu-

lation. Observational modeling by Kasper et al. (2017) have shown that the zone of preferential ion heating extends from the transition region out to $\sim 20\text{--}40 R_\odot$ from the Sun. In addition, the dissimilar heating of different ion species in the solar corona may provide important evidence for determining the heating mechanism(s), of which there are many speculated (Cranmer & van Ballegoijen 2003; Isenberg & Vasquez 2007; Zimbaro 2010; Artemyev et al. 2014), since there are statistical indications that the heating produces both mass-proportional and super-mass-proportional temperatures. Directly related to the results of the present simulation, Lee et al. (1986) and Lee & Wu (2000) have proposed a mechanism for the heating of protons and minor ions by fast shocks. They argue that protons and minor ions may be heated by multiple subcritical shocks ($M_A \lesssim 3$) produced by the eruptions of current sheets by microflares or stronger impulsive events before reaching a significant altitude in the corona and give rise to mild temperature anisotropies for protons. Their results also indicate that proton and ion heating is dependent on the mass/charge ratio due to the existence of a jump in the electric potential $\Delta\phi$ at the shock ramp. The results in the present paper provide evidence that fast-like shocks and subsequent preferential ion heating can occur without relying on eruptive current sheets. The observed preferential ion heating seen in the present simulation is undoubtedly dependent on the electric field and begins to occur near the point where the electric and thermal pressure forces experienced by the ions reach their maximum values. However the exact dynamics are complicated to analyze and would be better investigated using kinetic simulations.

3.2. Parameter Studies

Four parameter studies are undertaken in this subsection. The first study analyzes the effect the maximum shear speed V_{y0} has on the evolution of the system. The following two studies examine the effects the two-fluid plasma ratios, namely, the ion to electron mass ratio m_i/m_e and the speed of light to the base Alfvén speed ratio c/v_0 , have on the formation and characteristics of the shock. The last study is performed as a convergence test demonstrating that the chosen normalized value of d_i determined by varying d_i/L_0^{CL} does not affect the formation and the speed of the shock as a whole.

The values of the maximum shear velocities used in the first parameter study range from $0.00625v_0$ to $0.00125v_0$ and the two smallest values used, $0.0025v_0$ and $0.00125v_0$, put us well within the order of magnitude range of true photospheric shuffling speeds. All other variable values are kept the same as those used

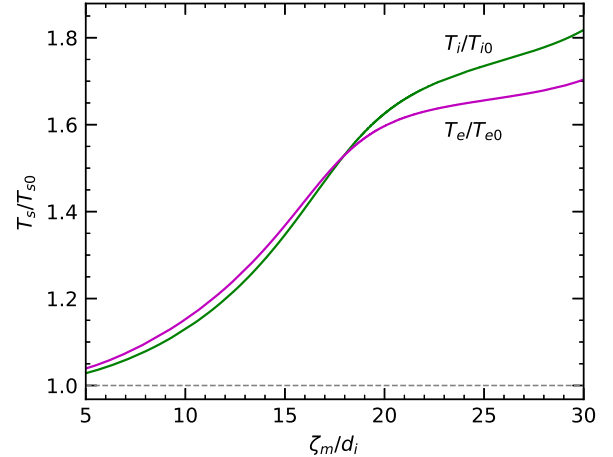


Figure 8. The ion (green) and electron (magenta) temperature ratios calculated at the shock as a function of ζ_m . The ratios are calculated with respect to the initial ion and electron temperatures.

in the representative case. Plot (a) in Figure 9 shows both the ion (solid lines) and electron (dashed lines) temperature ratios at the wavefront while the plot (b) exhibits the propagation velocities of the waves, v_p , for each of the shearing speeds adopted calculated along the z -axis. The most stark result from this study is that regardless of the maximum shearing speed applied, the propagation velocities of the waves along the z -axis before they exit the inner arcade are very nearly the same and then gradually begin to diverge relative to the maximum shearing speed applied for that simulation. This result is intriguing since the Poynting flux energy propagating into the computational domain from the base is proportional to the shearing speed. One might expect that the wave's propagation velocity would be directly proportional to the amount of energy driven into the system. This inconsistency can be explained by noting that even though the propagation velocity for all waves are approximately the same as they exit the inner region, the strengths of the discontinuities are proportional to the maximum shearing speed. Plot (a) in Figure 9 exhibits this point. Slower shearing speeds produce weaker heating effects which can be viewed as a proxy for a shock's strength. Therefore, slower shearing speeds produce weaker discontinuities and shocks with weaker compression at the wavefront between the upstream and downstream plasma. Lastly, it should be noted that the downstream velocity is also related to the strength of the shock. For the simulations of the two slowest shear speeds, the downstream velocities for the ions coming out of the shocks never exceeded the local Alfvén speed as viewed in the rest frame, but the propagation veloc-

ities of the waves for all simulations eventually surpass v_{fm} . The times where v_p just reaches the local v_{fm} are indicated by the crosses in the top plot of Figure 9.

For the mass ratio tests, the adopted value for the maximum shear speed is also that used in the representative case in §3.1. Figure 10 shows the influence of different values for the mass ratio m_i/m_e have on the strength of the extrema values and the spatial widths of the net charge profiles at the shock after it has formed taken at $\zeta_m = 17.25d_i$. Figure 10a illustrates that the widths between the net charge extrema always vary by only about two ion inertial lengths in the current gridding regardless of the value of the mass ratio. Figure 10b plots the magnitudes of the extrema values and the magnitudes adhere to a nearly linear relationship in the mass ratio. As the magnitude of the charge separation increases so too does the local strength of the electric field. Meanwhile, the mass ratios do influence the speeds of the shocks before saturating to their steady values

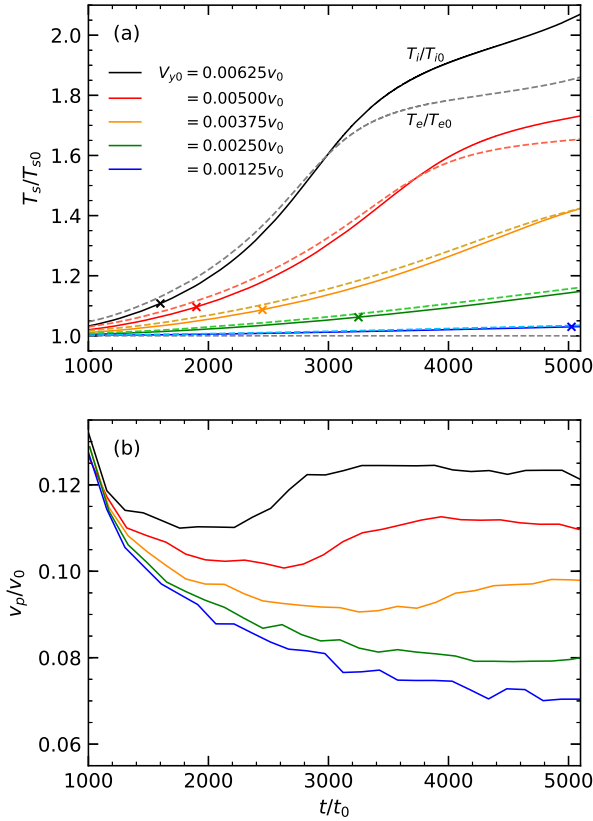


Figure 9. The ion (solid lines) and electron (dashed lines) temperature ratios at the wavefronts (a) and the velocities of the waves (b) calculated along the z -axis for 5 different values of the maximum shearing speed applied at the base. The crosses indicate the times the discontinuities have just reached the MHD fast mode velocity, v_{fm} , for that simulation.

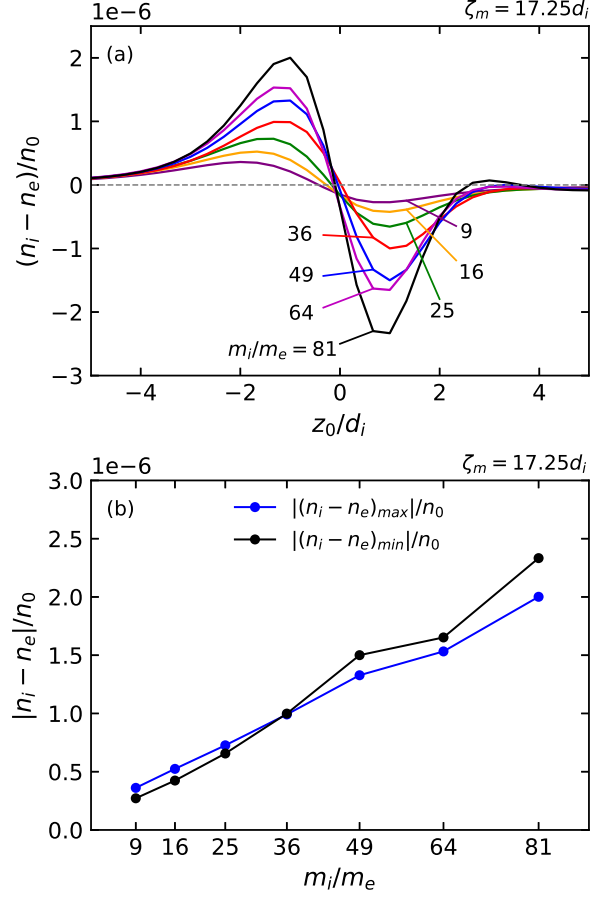


Figure 10. Plot (a) shows the net charge profiles $(n_i - n_e)/n_0$ for simulations with different values of the mass ratio m_i/m_e after the shock has formed in each simulation. The profiles are all aligned by the point z_0 representing the zero value between the net charge extrema. The magnitudes of the extrema values for the net charge are plotted in (b) and show that the magnitudes are linearly dependent on m_i/m_e .

and simulations with lighter electrons produce moderately faster moving waves. By the time the shock has saturated, the altitude achieved by the $m_i/m_e = 81$ simulated shock is nearly 5% higher compared to the shock observed in the $m_i/m_e = 9$ simulation, while the ratio of total mass between the $m_i/m_e = 9$ simulation and the $m_i/m_e = 81$ simulation is 9.8%. This effect is likely due to the greater saturation of electrons at the wavefront for larger values of the mass ratio. The larger accumulated electron density in the wavefront produces a stronger static electric force to accelerate the ions which would altogether be nonexistent in a purely MHD simulation.

For the third parameter study, we comment on the effects the speed of light to the base Alfvén speed ratio has on the formation of the shocks. The adopted test values are $c/v_0 = 10, 20,$ and 30 with V_{y0} and m_i/m_e

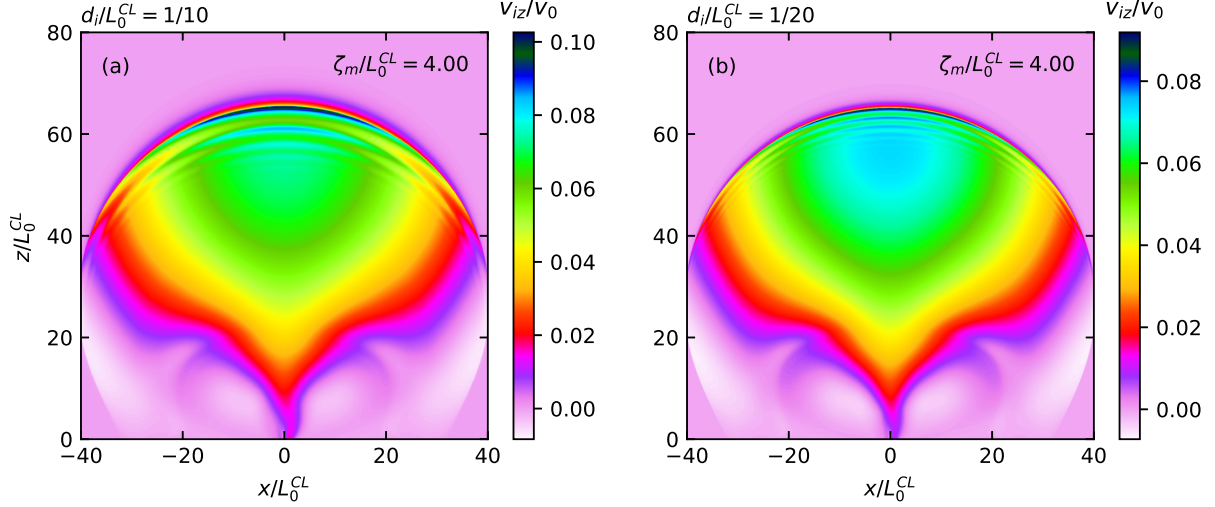


Figure 11. Snapshots of the discontinuities in the ion’s vertical motions, v_{iz} , for (a) $d_i/L_0^{CL} = 1/10$ and (b) $d_i/L_0^{CL} = 1/20$ after the shock has formed. The shock front recorded for $d_i/L_0^{CL} = 1/20$ is more abrupt than for the larger d_i case seen in (a). The length scale is normalized by L_0^{CL} instead of d_i .

set to the same values used in the representative case. It is observed that the ratio c/v_0 does not have any noticeable effect on the propagation speed of the discontinuities and shocks. However, c/v_0 does have an effect on the charge separation at the discontinuity, while simultaneously showing no strong effect on the strength of the electric field – the main accelerator for the ion fluid in the lower altitude regions. The weakened charge separation can be attributed to the varying response time that the plasma has to respond to disturbances, defined by $t_D = \lambda_D/v_{th} = 1/\omega_{pe}$ and after normalization is proportional to $t_D \propto 1/(c/v_0)$, where λ_D and v_{th} are the Debye length and electron thermal velocity, respectively, defined in the usual sense. If the plasma experiences a perturbation, the plasma will react in a characteristic time t_D . As seen in the simulations for this parameter study, the plasma reacts more quickly to perturbations in the charge separation and as a result the accumulated net charge at the discontinuity is lower for larger values of the speed of light, since t_D has an inverse dependence on the ratio c/v_0 . Meanwhile, in the simulation’s computational scheme, Gauss’s law takes on the normalized form $\nabla \cdot \mathbf{E} = (c/v_0)^2(n_i - n_e)$. The reduced strengths of the charge separation observed in the simulations are of the same order of magnitude as the inverse of the adopted value of $(c/v_0)^2$. Therefore, the variances in $(c/v_0)^2$ and $(n_i - n_e)$ nullify one another and the divergence of the electric field remains unchanged regardless of the adopted value of c/v_0 .

In the final parameter study, the formation and characteristics of the discontinuities and shocks are investigated for their dependence on the normalized ion in-

ertial length by varying the ratio of d_i to the Choe & Lee (1996a,b) arcade length scale, L_0^{CL} . The values of this ratio adopted for this study were $d_i/L_0^{CL} = 1/5, 1/10, 1/20$, and $1/30$, while m_i/m_e and c/v_0 remained the same with those adopted in §3.1. The resolution for individual spans of d_i is kept constant for each simulation and necessarily stipulates that the number of total grid points scale by $(d_i/L_0^{CL})^{-2}$. In order to reduce the amount of computation time, the maximum shear velocity applied was twice that adopted in the representative case, i.e., $V_{y0} = 0.01v_0$ and the computational domain was halved. The significance of this study is to examine whether the artificially increased ion in-

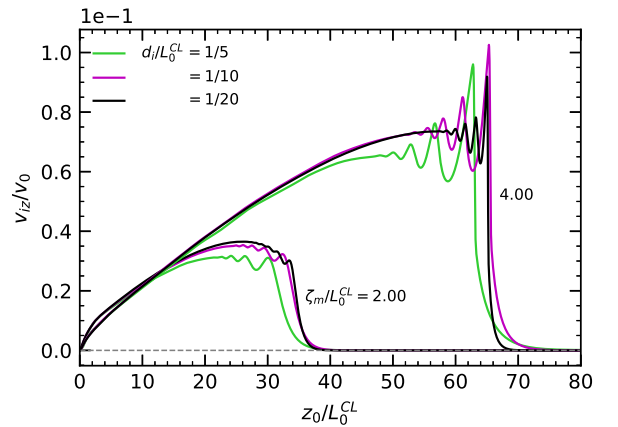


Figure 12. Profiles of the ion’s vertical motions along the z -axis recorded in simulations for varying d_i/L_0^{CL} at two different values of maximum shear. The wave steepening is greater for smaller values of d_i . The length scale is normalized by L_0^{CL} .

tial length d_i also artificially enhances the generation of the propagating discontinuities and shocks discussed previously. The downstream region of the shock remains unchanged for different values of d_i/L_0^{CL} except in the immediate downstream as exhibited in Figure 11. Figure 12, which plots profiles of v_{iz} along the z -axis, illustrates that in the immediate downstream regions the width of the disturbance amplitudes trailing the shock front are nearly proportional to the normalized value of d_i . This is not an effect of having a higher resolution for simulations with smaller dimensional values of d_i since a convergence study for the $d_i/L_0^{CL} = 1/10$ case with triple the grid points showed the same behavior as the $d_i/L_0^{CL} = 1/10$ shown in Figures 11 and 12. In the immediate downstream region, the amplitude of the trailing disturbances is slightly greater with a comparatively larger width among local maxima for greater values of d_i . This seems to suggest that the charge separation effects require a longer amount of time to manifest for smaller values of d_i , however this does not have an effect on the formation of the shock as a whole. In fact, Figure 12 shows that steepness or abruptness of the shock discontinuity is greater for smaller values of d_i . As for the speed of the shock, it remains nearly the same for all cases undertaken with the slowest shock speed seen in the simulation with the largest value of d_i . Meanwhile, the compression and thermal ratios for each shock seen in this study also were nearly universal across the simulations. The results of the current parameter study do not indicate that d_i has a large effect on the formation of the shock as a whole, except small varying qualitative behavior in the immediate downstream region.

4. CONCLUSION

In this study, the dynamic evolution of a magnetic arcade associated with photospheric shearing motions was investigated by an ideal two-fluid (electron-ion) code. The two-fluid numerical simulations produce conspicuous differences compared to earlier ideal and resistive MHD simulations beyond the inner arcade region with the formation of a fast outwardly propagating wave that eventually steepens into a shock. The decoupling motion between the electrons and heavier ions as the arcade expands induces a growing charge separation and strong electric field gradients in the front of the arcade manifested by a larger saturation of electrons at the wavefront followed by the lagging ions. The charge separation induced electric field provides an additional force, along with the magnetic and thermal pressures, that drive the growth of an expanding wave that steepens into propagating discontinuities in the plasma and field values and provides the bulk of the ion acceleration in the ini-

tial stages. The propagation speed of this wave eventually exceeds the local phase velocity of the MHD fast mode, v_{fm} , and the observed discontinuities are classified as a perpendicular fast-like shock driven by the shearing motions at the base that propagates across the local magnetic field. The strong compression seen at the shock front heats both the ion and electron fluids, however trailing the shock wave this heating is eventually extinguished by cooling that is caused by the fast adiabatic expansion of the magnetic arcade. Directly after the vertical velocity of the ions exceeds that of the electrons at the shock, preferential heating in the ions is first observed. In addition, parameter tests indicate that (1) the propagation speed of the shock is independent of the maximum shear speed; (2) slower shearing speeds produce weaker shocks with weaker adiabatic heating; (3) the ion to electron mass ratio, m_i/m_e , impacts the strength of the charge separation linearly, but has a moderate effect on the propagation speed; and (4) the normalized value of the ion inertial length does not affect the formation and the speed of the shock as a whole.

The qualitatively similar behavior for all simulations performed in the convergent study with varying adopted values of d_i is taken as evidence that artificially increasing d_i to a computationally practical size compared to the global length scale of the arcade l_0 with $l_0 \gg d_i$ still maintains physical relatability and authenticity for the evolution of a full-size magnetic arcade structure. The simulations undertaken in this study demonstrate that multi-fluid effects can affect the global evolution of the corona driven simply by gradual and steady local motions much more so than observed in purely MHD simulations. This point is interesting since the footpoint motions of magnetic structures tied at the photosphere are dynamical so that the cumulative multi-fluid effects of many magnetic structures undergoing footpoint motions simultaneously could be significant. Lastly, in a future study we plan to modify the current code to simulate for larger values of maximum shear ζ_m and analyze the two-fluid evolution of the current sheet formation and the anticipated magnetic reconnection in the central arcade region.

Acknowledgements. This work was supported by the National Natural Science Foundation of China under Grant No. 11775188 and 11835010, the Special Project on High-Performance Computing under the National Key R&D Program of China No. 2016YFB0200603, the Fundamental Research Fund for Chinese Central Universities, and the Chinese Scholarship Council's (CSC)

Chinese Government Scholarship for International Students (CSC No. 2017DFJ005297).

REFERENCES

- Aly, J. J. (1984), On some properties of force-free magnetic fields in infinite regions of space, *ApJ*, 283:349
- Amari, T., J. F. Luciani, J. J. Aly, M. Tagger (1996), Plasmoid formation in a single sheared arcade and application to coronal mass ejections, *A&A*, 306, 913
- Artemyev, A. V., G. Zimbardo, A. Y. Ukhorskiy, M. Fujimoto (2014), Preferential acceleration of heavy ions in the reconnection outflow region, *A&A*, 562, A58
- Biskamp, D., Schwarz, E., Drake, J. F. (1995), Ion-controlled collisionless magnetic reconnection, *Phys. Rev. Lett.*, 75:3850
- Choe, G. S. & Lee, L. C. (1996a), Evolution of solar magnetic arcades. I. Ideal MHD evolution under footpoint shearing, *ApJ*, 472:360
- Choe, G. S. & Lee, L. C. (1996b), Evolution of the solar magnetic arcades. II. Effect of resistivity and solar eruptive processes, *ApJ*, 663:1363
- Cranmer, S. R. & A. A. van Ballegoijen (2003), Alfvénic turbulence in the extended solar corona: kinetic effects and proton heating, *ApJ*, 594:573
- de Hoffman, F. & Teller, E. (1950), Magneto-hydrodynamic shocks, *Phys. Rev.*, 80, 692
- Forbes, T. G. (2000), A review on the genesis of coronal mass ejections, *J. Geophys. Res.*, Vol. 105, No. A10, pg 23,153-23,165
- Hsieh, M. H., C. L. Tsai, Z. W. Ma, L. C. Lee (2009), Formation of fast shocks by magnetic reconnection in the solar corona, *PoP*, Vol.16, 092901
- Isenberg, P. A. & Vasquez, B. J. (2007), Preferential perpendicular heating of coronal hole minor ions by the Fermi mechanism, *ApJ*, 668:546
- Kaspar, J. C., K. G. Klein, T. Weber, M. Maksimovic, A. Zaslavsky, S. D. Bale, B. A. Maruca, M. L. Stevens, A. W. Case (2017), A Zone of Preferential Ion Heating Extends Tens of Solar Radii from the Sun, *ApJ*, 849:126
- Klimchuk, J. A. (2001), Theory of coronal mass ejections, *Space Weather*, Geophysical Monograph 125
- Kuperus, M., J. A. Ionson, D. S. Spicer (1981), On the theory of coronal heating mechanisms, *Ann. Rev. Astron. Astrophys.*, 19:7
- Landi, E. (2007), Ion temperatures in the quiet corona, *ApJ*, 663:1363
- Lee, L. C., C. S. Wu, X. W. Hu (1986), Increase of ion kinetic temperature across a collisionless shock: I. A new mechanism, *Geophys. Res. Lett.*, 13:209
- Lee, L. C. & Wu, B. H. (2000), Heating and acceleration of protons and minor ions by fast shocks in the solar corona, *ApJ*, 535:1014
- Ma, Z. W., Bhattacharjee, A. (1996), Fast impulsive reconnection and current sheet intensification due to electron pressure gradients in semi-collisional plasmas, *Geophys. Res. Lett.*, 23:1673
- Masuda, S., T. Kosugi, H. Hara, S. Tsuneta, Y. Ogawara (1994), A loop-top hard X-ray source in a compact solar flare as evidence for magnetic reconnection, *Nature*, 371:495
- Mikić, Z., D. C. Barnes, D. D. Schnack (1988), Dynamical evolution of a solar coronal magnetic field arcade, *ApJ*, 328:830
- Mikić, Z. & Linker, J. A. (1988), Disruption of coronal magnetic field arcades, *ApJ*, 430:898
- Orta, J. A., M. A. Huerta, G. C. Boynton (2003), Magnetohydrodynamic shock heating of the solar corona, *ApJ*, 596:646
- Osterbrock, D. E. (1961), The heating of the solar chromosphere, plages, and corona by magnetohydrodynamic waves, *ApJ*, 134:347
- Sears, F. W. (1953), Thermodynamics, the kinetic theory of gases, and statistical mechanics, Addison-Wesley: Reading, MA, pg. 3
- Sen, A. K. & Spero, D. M. (1967), Jump conditions for a two-fluid plasma, *Phys. Fluids*, 10, 1597
- Steinolfson, R. S. (1991), Coronal evolution due to shear motion, *ApJ*, 382:677
- Sturrock P.A. (1991) Maximum energy of semi-infinite magnetic-field configurations. In: Uchida Y., Canfield R.C., Watanabe T., Hiei E. (eds) Flare Physics in Solar Activity Maximum 22. Lecture Notes in Physics, vol 387. Springer, Berlin, Heidelberg
- Takasao, S., A. Asai, H. Isobe, K. Shibata (2012) Simultaneous observation of reconnection inflow and outflow associated with the 2010 August 18 solar flare, *ApJL*, 745:L6
- Woods, L.C. (1969), Jump conditions for a two-fluid magneto-plasma, *Plasma Phys.*, 11, 967
- Yamada, M., R. Kulsrud, H. T. Ji (2010), Magnetic reconnection, *Rev. Mod. Phys.*, 82, 603
- Zhang, Q. M. & Ni, L. (2019), Subarcsecond Blobs in Flare-related Coronal Jets, *ApJ*, 870:113

- Zimbardo, G. (2010), More than Mass Proportional Heating of Heavy Ions by Collisionless Quasi-Perpendicular Shocks in the Solar Corona, AIP Conference Proceedings 1216, 52
- Zimbardo, G. (2011), Heavy ion reflection and heating by collisionless shocks in polar solar corona, Planet. Space Sci., Vol. 59, 7, 468